Arabian Journal of Chemistry (2021) **14**, 103058

King Saud University

Arabian Journal of Chemistry

www.ksu.edu.sa
www.sciencedirect.com

ORIGINAL ARTICLE

Novel bimodal micro-mesoporous $Ni_{50}Co_{50}$-LDH/UiO-66-NH_2 nanocomposite for Tl(I) adsorption

Roozbeh Soltani [a], Rasool Pelalak [b,c], Mahboubeh Pishnamazi [b,d], Azam Marjani [e,f,*], Shaheen M. Sarkar [g], Ahmad B. Albadarin [g], Saeed Shirazian [g,h]

[a] *Department of Chemistry, Islamic Azad University, Arak Branch, Arak, Iran*
[b] *Institute of Research and Development, Duy Tan University, Da Nang 550000, Viet Nam*
[c] *Faculty of Environmental and Chemical Engineering, Duy Tan University, Da Nang 550000, Viet Nam*
[d] *The Faculty of Pharmacy, Duy Tan University, Da Nang 550000, Viet Nam*
[e] *Department for Management of Science and Technology Development, Ton Duc Thang University, Ho Chi Minh City, Viet Nam*
[f] *Faculty of Applied Sciences, Ton Duc Thang University, Ho Chi Minh City, Viet Nam*
[g] *Department of Chemical Sciences, Bernal Institute, University of Limerick, Limerick, Ireland*
[h] *Laboratory of Computational Modeling of Drugs, South Ural State University, 76 Lenin prospekt, 454080 Chelyabinsk, Russia*

Received 27 December 2020; accepted 31 January 2021
Available online 10 February 2021

KEYWORDS

Adsorbent;
In situ growing;
Isotherm studies;
Metal-organic frameworks;
Surface functionalization;
Thermodynamics

Abstract $Ni_{50}Co_{50}$-layered double hydroxide/UiO-66-NH_2 metal–organic framework nanocomposite ($Ni_{50}Co_{50}$-LDH/UiO-66-NH_2 NC) was synthesized through a facile ultrasonic-assisted hydrothermal method. UiO-66-NH_2 MOF nanocrystals were *in situ* grown on the surface of ultrathin 2-dimensional functionalized $Ni_{50}Co_{50}$-LDH nanosheets. Using this method, a uniform nanocomposite architecture was obtained by uniformly distributing MOF nanocrystals on $Ni_{50}Co_{50}$-LDH. The synthesized LDH/MOF NC possesses essential properties of potential nanoadsorbent such as high surface area (907 $m^2\ g^{-1}$), large pore volume (0.91 $cm^3\ g^{-1}$), bimodal micro-mesoporous structure, and chemical functionality. Accordingly, $Ni_{50}Co_{50}$-LDH/UiO-66-NH_2 NC was used as an adsorbent for the uptake of toxic thallium (I) from water. Isotherm, thermodynamic, and kinetic studies were conducted to gain a better insight into the adsorption mechanism (s) involved in the removal process. Langmuir and pseudo-first-order models present a better fit to the isotherm and kinetic data, respectively, and the maximum Langmuir adsorption capacity was found to be 601.3 mg g^{-1} after non-linear fitting analysis (pH = 7.0, solution volume = 30 mL, initial thallium (I) concentration = 50 mg L^{-1}, contact time = 15 min, solution temperature = 293 K).

* Corresponding author at: Ton Duc Thang University, Ho Chi Minh City, Viet Nam.
E-mail address: azam.marjani@tdtu.edu.vn (A. Marjani).

Peer review under responsibility of King Saud University.

Production and hosting by Elsevier

https://doi.org/10.1016/j.arabjc.2021.103058

Thermodynamic parameters were estimated ($\Delta H^0 = +64.979$ kJ mol^{-1}, $\Delta S^0 = +0.335$ kJ mol^{-1} K^{-1}, $\Delta G^0 = -33.176$ to -39.876 kJ mol^{-1}) and it was found that the adsorption is endothermic and spontaneous with a physicochemical adsorption nature.

1. Introduction

Highly toxic heavy metals such as thallium (Tl), chromium (Cr), cadmium (Cd), lead (Pb), mercury (Hg), arsenic (As), and manganese (Mn) cause significant health effects in both humans and animals. Among them, Tl with a relative atomic mass of 204.37 and a density of 11.83 g cm^{-1} is a highly toxic heavy metal and even more poisonous to mammals than many other heavy metals like Pb, Cd, Hg, Cu, and Zn. Accordingly Tl rates as an Environmental Protection Agency (EPA) priority pollutant with a maximum permissible concentration of 2 μg L^{-1} in drinking water (Peter and Viraraghavan, 2005). From the viewpoint of ecotoxicological and health importance, exposure to a low level of Tl(I) can cause diseases as well as various disorders, such as headache, psychic disturbance, alopecia, acute progressive paralysis, anorexia, temporary hair loss, and even cardiovascular effects, because it is easily absorbed through the skin and mucous membrane and accumulated in bones, renal medulla, and central nervous system (Cvjetko et al., 2010; Sangvanich et al., 2010; Dashti Khavidaki and Aghaie, 2013). Tl is a ubiquitous trace element, which has an average concentration of 0.013 mg L^{-1} in the oceanic crust, and 0.49 mg L^{-1} in the continental crust and has been used to manufacture scintillation counters for radioactivity quantitation, infrared spectrometers, ceramic semiconductor material, pigments (thallium chromate), imitation jewelry, catalyst, and low-temperature thermometers (Peter and Viraraghavan, 2005; Wan et al., 2014). Tl has been released into the environment (soil, water, and wastewater) by anthropogenic activities such as smelting and coal combustion, exploiting and machining mines, as well as other thriving industries, ranging from dozens of μg L^{-1} to several mg L^{-1} (Dashti Khavidaki and Aghaie, 2013; Twidwell and Williams-Beam, 2002). Consequently, removing Tl from aquatic environments and aqueous media, and controlling its contamination regarding humans and the environment is indispensable.

Current approaches to remove heavy metals pollutants from the aquatic environment include filtration, reverse osmosis, solvent extraction, chemical precipitation, electrochemical removal, etc. However, these techniques have disadvantages such as high energy consumption, incomplete removal, high-cost procedure, production of secondary pollution, process complexity, the need for specialized operators, sludge production, and the use of organic solvents in the process (Burakov et al., 2018; Carolin et al., 2017; Azimi et al., 2017). As a more general problem, these methods suffer from high selectivity for removing heavy metals. For these reasons, these methods are commonly used together during a remediation process. The adsorption method is another approach to removing heavy metals and other pollutants from water and wastewater and has attracted increasing attention in recent years (Pelalak et al., 2021; Marjani et al., 2020; Pelalak et al., 2021). The advantages of this method compared to the techniques mentioned above include designability, selectivity, lower costs, lack of sludge, lower energy consumption, and simplicity of the process (Burakov et al., 2018; Soltani et al., 2020; Soltani et al., 2020; Soltani et al., 2020; Yanyan et al., 226 (2018); Albadarin et al., 2017).

In recent years, nanomaterials including layered double hydroxides (LDHs) (Soltani et al., 2018; Zubair et al., 2017), metal–organic frameworks (MOFs) (Feng et al., 2018; Khan et al., 2013; Madden et al., 2020) covalent organic frameworks (COFs) (Li et al., 2018; Wang and Zhuang, 2019; Heydari et al., 2021); mesoporous silica and carbon materials (MSMs and MCMs) (Soltani et al., 2020; Soltani et al., 2019; Soltani et al., 2020; Gang et al., 2021); graphene and graphene oxides (Lim et al., 2018; Zhang et al., 2020), and polymer matrix nanocomposites (PMNCs) (Soltani et al., 2020; Zabihi et al., 2020; Zarei et al., 2019) have shown their potential as promising adsorbents. Among them, MOFs arouse worldwide interest during the past decade because of their remarkable properties including high surface area, regular porosity, designable structure, and dense aromatic linkers (Soltani et al., 2020; Zhang et al., 2019). Recently, among various kinds of MOFs, water-resistant functionalized MOFs such as UiO-66-NH_2, UiO-66-(Zr)-$(COOH)_2$, and NH_2-MIL-68, have attracted more and more attention both because of the presence of functional groups (hydroxyl, amine, carboxyl, and thiol) in their structure and the ability to use them in the presence of moisture or water (Zhang et al., 2019; Wang et al., 2020; Yang et al., 2013; Soltani et al., 2021; Shi et al., 2020). LDHs are another group of nanomaterials that have received considerable interest among researchers, especially those who work on the environmental applications of LDHs (Soltani et al., 2018; Soltani et al., 2020; Yang et al., 2020; Yang et al., 2020). However, the most important disadvantages of LDHs and MOFs as adsorbents are low surface area and small particle size (nanometer-size particles), respectively (Soltani et al., 2021). The low surface area of an adsorbent restricts access to the adsorption sites and the small particle size of adsorbent particles makes it difficult to separate them from the aqueous medium (generally needs high-speed centrifugation). Nevertheless, the simultaneous use of these two unique structures in the form of a composite can combine the properties and advantages of both materials and create a composite with hybrid features. Furthermore, by choosing the right strategy, it is possible to prepare a composite of LDH and MOF which solves the two aforementioned disadvantages, namely low surface area and small particle size of the adsorbent. Recently, we found that very few reports have been made on the synthesis and development of these hybrid LDH/MOF structures for practical applications especially adsorption and extraction. For instance, in 2017, Yang et al. (Yang et al., 2017) reported a method for *in situ* growth of Zeolite ZIF-8 MOF on Zn-Al LDH to prepare a ZIF-8/LDH nanocomposite

for As^V removal from aqueous media. In 2018, Hu et al. (Hu et al., 2018) reported the preparation of ZIF-8/Zn-Al layered double oxides composite (LDO) using an *in situ* growth approach for photocatalytic degradation of an organic dye. In these works, Zn-Al LDH was fabricated by the co-precipitation of zinc and aluminum nitrate salts in the presence of urea. Although these LDO/MOF and LDH/MOF nanocomposites revealed acceptable performance for adsorption and degradation applications, the following drawbacks to these LDH/MOF nanocomposites are worth considering:

(1) The surfaces of the Zn-Al LDH and Zn-Al LDO, as a scaffold, were not homogeneously covered by MOF nanoparticles. This might be due to the presence of impurities that influenced the growth of MOF nanoparticles on the rough surfaces of Zn/Al LDH material (Yang et al., 2017).
(2) Due to the lack of strong chemical bonds between the two components, there is a possibility of separation of LDH and MOF nanoparticles caused by environmental factors or ultrasonic waves during the adsorption and desorption procedures.
(3) The Zn-Al LDH and Zn-Al LDO particles used are only a few micrometers in size, which results in the production of adsorbents with very fine particles, which in turn complicate the process of separating the adsorbent from the aqueous media.
(4) The lack of organic functional groups (–OH, –NH, –SH, –C = O) as active adsorption sites on the pores and surface of the MOF nanoparticles potentially leads to a decrease in adsorption performance of the LDO/MOF and LDH/MOF adsorbents in comparison with their functionalized-homologs.

In 2020, Soltani and colleagues (Soltani et al., 2020) reported the synthesis of an LDH/MOF composite with a hierarchical trimodal *micro-meso-macro* porosity as a superior adsorbent for simultaneous adsorption of Cr(VI) and orange II reactive dye, in which bimetallic zeolitic imidazole frameworks (BMZIF20) uniformly grow on the surface of $Ni_{50}Co_{50}$-LDH nanosheets. In order to establish strong chemical bonds between the LDH surface and MOF nanocrystals, the surface of the LDH was first modified with an appropriate silane coupling agent and then MOF nanocrystals were *in situ* grown on the LDH surface. Another important point in this work compared to the method used by the aforementioned works is the use of the $Ni_{50}Co_{50}$-LDH with extended 2D ultrathin nanosheets, which can play the role of an appropriate scaffold for growing MOF nanocrystals. Although the method reported by Soltani and colleagues solves the three above-mentioned shortcomings (drawbacks 1–3), the problem of functionality (problem 4) remains unresolved. In 2021, Soltani and co-workers (Soltani et al., 2021) reported the synthesis of an LDH/MOF composite *via* a facile and "green" synthesis approach in which UiO-66-(Zr)-$(COOH)_2$ nanoparticles were *in situ* grown on the surface of carboxylic-functionalized $Ni_{50}Co_{50}$-LDH sheets in water as solvent under reflux condition. Although this reported LDH/MOF composite possesses abundant amine and carboxylic functional groups in its hierarchical structure and solved the problem of functionality, the LDH/MOF adsorbent does not possess a high surface area (surface area = 41 $m^2\ g^{-1}$).

Here, for the first time, in line with our previous research and with the aim of solving the problem of functionality, a novel $Ni_{50}Co_{50}$-layered double hydroxide/UiO-66-NH_2 metal–organic framework nanocomposite (denoted as $Ni_{50}Co_{50}$-LDH/UiO-66-NH_2 NC) was synthesized using *in situ* growth of amine-decorated MOF nanocrystals on the surface of functionalized-$Ni_{50}Co_{50}$-LDH under a mild hydrothermal condition. Due to the presence of abundant adsorption groups in the $Ni_{50}Co_{50}$-LDH/UiO-66-NH_2 NC structure, this material was used as an adsorbent to remove Tl(I) cations from the aqueous solution and its adsorption performance was systematically investigated.

2. Experimental section

2.1. Materials

2-Aminoterephthalic acid (2-amino-1,4-benzenedicarboxylic acid, H_2N-H_2BDC, 99%), zirconium(IV) chloride ($ZrCl_4$, ≥99.5%), cobalt(II) nitrate hexahydrate ($Co(NO_3)_2$ṡ$6H_2O$, ≥98%), nickel(II) nitrate hexahydrate ($Ni(NO_3)_2$ṡ$6H_2O$, ≥98.5%), and (3-chloropropyl)trimethoxysilane (CPTMS, ≥97%) were purchased from Sigma-Aldrich (Germany). Thallium(I) nitrate ($TlNO_3$, ≥99.9%), urea (≥99.5%), ethylene glycol (EG, ≥99.5%), fuming hydrochloric acid (HCl, 37%), sodium hydroxide pellets (NaOH, ≥99%), acetone (≥99.8%), ethanol (absolute), N, N-dimethylformamide (DMF, ≥99.8%), and toluene (≥99.9%) were purchased from Merck (Germany). Ethanol (96% v/v) was purchased from Dr. Mojallali Chemical Laboratories (Tehran, Iran). Double-distilled water (DDW) was used for the synthesis of materials and Tl(I) adsorption experiments.

2.2. Synthesis of the samples

2.2.1. Synthesis of $Ni_{50}Co_{50}$-LDH ultrathin nanosheets

$Ni_{50}Co_{50}$-LDH was synthesized according to the large-scale preparation and environmentally-friendly synthetic method described by Soltani and co-workers (Soltani et al., 2018; Soltani et al., 2020). For a typical synthesis, 90 mL EG and 36 mL DDW were added into a 250 mL round-bottom flask containing 12.0 mmol (3.492 g) $Co(NO_3)_2$ṡ$6H_2O$ and 6.0 mmol (1.745 g) $Ni(NO_3)_2$ṡ$6H_2O$ (Co:Ni = 2:1), and the mixture was magnetically stirred until the entire salts were dissolved. Once the temperature of the reaction mixture reached 363 K, 90 mmol (5.405 g) urea was added to the flask, and the mixture was magnetically stirred under reflux for 3 h at 363 K. After cooling the mixture to room temperature (RT), the green precipitates were filtered through a Whatman No. 42 filter paper by means of vacuum filtration and repeatedly rinsed with DDW and ethanol 96% to eliminate the remains of reactants and EG. The pale green $Ni_{50}Co_{50}$-LDH ultrathin nanosheets were obtained after oven-drying the precipitates at 333 K for 24 h.

2.2.2. Synthesis of $Ni_{50}Co_{50}$-LDH-Cl

Post-modification of $Ni_{50}Co_{50}$-LDH was carried out by adding a certain amount of CPTMS into a 250 mL round-bottom flask containing 100 mL dry toluene and 1.00 g synthesized $Ni_{50}Co_{50}$-LDH, followed by ultrasonication (15 min, RT),

refluxing under stirring (N_2 atmosphere, 383 K, 24 h), repeatedly washing (toluene and acetone), and drying (under vacuum at RT overnight and 343 K for another 12 h).

2.2.3. Synthesis of UiO-66-NH_2

UiO-66-NH_2 was prepared according to the method described by Lillerud and co-workers with a slight modification (Kandiah et al., 2010). In a volumetric flask, 9.6 mmol (1.739 g) H_2N-H_2BDC and 9.6 mmol $ZrCl_4$ (2.237 g) were dissolved in 200 mL DMF at RT and the flask was transferred to a preheated electric oven at 353 K overnight and then held at 373 K for 1 day. After cooling the mixture to RT, the obtained solid was filtered through a Whatman No. 42 filter paper using vacuum filtration and rinsed several times with absolute ethanol for 2 days while heated at 333 K in a water bath. Finally, the obtained yellow powder was separated using vacuum filtration, transferred to a Schlenk flask, and oven-dried under vacuum at RT.

2.2.4. Synthesis of $Ni_{50}Co_{50}$-LDH/UiO-66-NH_2 NC

2.25 g $Ni_{50}Co_{50}$-LDH-Cl was added into a volumetric flask containing 150 mL dry DMF and the mixture was ultrasonicated for 15 min at RT. Then, a mixture containing 9.6 mmol H_2N-H_2BDC and 9.6 mmol $ZrCl_4$ in 100 mL dry DMF was added to the above mixture and stirred for 15 min at RT. Afterward, the volumetric flask was sealed and transferred in a preheated electric oven at 353 K overnight and then held at 373 K for a day. Finally, the reaction mixture was cooled to RT, filtered, washed with absolute ethanol, and dried as mentioned in the previous section.

After the synthesis of the aforementioned samples, the residual solvents (DMF, ethanol, toluene, and acetone) were distilled and purified according to the known procedures.

2.3. Characterization of the samples

Powder X-ray diffraction (XRD) measurements were performed on the samples at ambient atmosphere and 293 K on a Bruker D5000 (Siemens, Germany) diffractometer using monochromatic Cu Kα radiation (λ = 1.540 A°).

The molecular bond structure and chemical nature of the samples were studied using Fourier transform infrared (FTIR, Thermo Nicolet, Avatar 330 FTIR Spectrometer, USA) spectroscopy in the wavelength range of 4000 cm^{-1}-400 cm^{-1} by making 60 scans at a resolution of 4 cm^{-1}.

The microscopic observations and energy dispersive spectroscopy (EDS)-Mapping were performed by a Field Emission Scanning Electron Microscope (FESEM, MIRA3 TESCAN-XMU, Kohoutovice, Czech Republic).

N_2 adsorption–desorption measurements at 77 K was carried out using a porosimetry analyzer (Belsorp-mini II, BEL Japan). The Langmuir, Brunauer-Emmett-Teller (BET), and t-plot equations were used to estimate the surface area of the samples. The pore diameter (D) of the samples was calculated using nonlocal density functional theory (NLDFT).

The concentrations of Tl(I) cations in aqueous media were measured using a flame atomic absorption spectrophotometer (FAAS - SHIMADZU AA 6800 model).

2.4. Adsorption experiments

Batch adsorption tests for Tl(I) adsorption by $Ni_{50}Co_{50}$-LDH/UiO-66-NH_2 NC were conducted in a thermostatically controlled shaking water bath (Precision Scientific Inc., Chicago, IL) using traditional bottle-point method in 100-mL narrow-mouth polypropylene (PP) bottles. $TlNO_3$ was dissolved in DDW to form Tl(I) stock solution (1000 mg L^{-1}). The working solutions were prepared daily from the stock solution with DDW. The effect of some important factors such as solution pH, adsorbent dose (W), initial Tl(I) concentration (C_i), contact time (t), and temperature (T) on the adsorption process were systematically monitored.

The adsorption capacity and removal percentage were calculated using equations (1–3) in Table 1. Different non-linear isotherm (Eqs. (4–6)) equations, thermodynamic equations (Eqs. (7–9)), and non-linear kinetic (Eqs. (10–12)) equations were used for predicting adsorption mechanism (s) and the probable interactions between Tl(I) cations and the adsorbent. Non-linear regression analysis (NLRA) was used in this work for fitting the isotherm and kinetic data by using the statistical analysis function in Origin Pro 8.6 software (Origin Lab Corporation, Northampton, USA).

It is reported that the non-linear method is a more appropriate method than the linear method to estimate either the isotherm parameters or kinetic parameters because in the non-linear analysis technique the error distribution does not get altered as in the linear analysis method (Soltani et al., 2020; Soltani et al., 2020; Kumar and Sivanesan, 2006; Soltani et al., 2019).

The detailed experimental procedures for adsorption of Tl (I) by $Ni_{50}Co_{50}$-LDH/UiO-66-NH_2 NC were illustrated in the following sections.

2.4.1. The effect of pH and adsorbent dose

The simultaneous influence of pH and adsorbent dose on Tl(I) adsorption by the adsorbent was investigated first. The pH of a 30 mL solution containing 30 mg L^{-1} of Tl(I) cations and a certain dose of the adsorbent (W = 0.001, 0.002, and 0.005 g) was adjusted to a target set between 5.5 and 8.5 using 0.01 mol L^{-1} NaOH and HCl. After shaking for 120 min (T = 293 K, shaking speed = 180 rpm), samples were taken and the powder adsorbent was isolated from the solution by centrifugation, and then the Tl(I) concentration was measured immediately using FAAS.

2.4.2. The effect of initial Tl(I) concentration and temperature

For isotherm and thermodynamic studies, the initial concentration of Tl(I) cations and temperature values were varied from 0.5 to 250 mg L^{-1} and 293 to 313 K, respectively. The samples (pH = 6.5, V = 30 mL, W = 0.002 g) were shaken for 120 min and then taken and centrifuged and the residual metal concentration in the supernatant was measured immediately afterward.

2.4.3. The effect of contact time

For kinetic studies, the solutions (pH = 6.5, V = 30 mL, W = 0.002 g, T = 303 K) were shaken and samples were taken

Table 1 Adsorption equations (isotherm, kinetic, and thermodynamic equations).

Equations	Parameters (units)
$\%R = \frac{C_i - C_e}{C_i} \times 100$(1)	C_i: initial concentration (mg L^{-1}) C_e: equilibrium concentration (mg L^{-1})
$q_t = (C_i - C_t) \times \frac{V}{W}$(2) $q_e = (C_i - C_e) \times \frac{V}{W}$(3)	q_t: adsorption capacity at any time t (mg g^{-1}) q_e: equilibrium adsorption capacity (mg g^{-1}) V: solution volume (mL) W: adsorbent dose (mg)
Langmuir : $q_e = \frac{q_{m,cal.} \cdot K_L \cdot C_e}{1+(K_L \cdot C_e)}$(4)	$q_{m,cal.}$(mg g^{-1}): calculated maximum adsorption capacity K_L (L mg^{-1}): Langmuir isotherm constant $R_L = [1/(1 + K_L \cdot C_0)]$, R_L (dimensionless): separation factor
Freundlich : $q_e = K_F \cdot C_e^{1/n}$(5)	K_F (mg g^{-1})(L $g^{-1})^n$: Freundlich isotherm constant related to the adsorption capacity n (dimensionless): adsorption intensity
R − P : $q_e = \frac{K_{R-P} \cdot C_e}{1+(\alpha_{R-P} \cdot C_e^g)}$(6)	K_{R-P} (L g^{-1}): Redlich-Peterson isotherm constant α_{R-P} (L mg^{-1}): Redlich-Peterson isotherm constant g (dimensionless): Redlich-Peterson isotherm binding constant, $0 < g < 1$
$K_e^0 = \frac{[adsorbate]^0 \cdot MW \cdot K_L \cdot 1000}{\gamma}$(7)	K_e^0(dimensionless): thermodynamic equilibrium constant $[adsorbate]^0$ (1 mol L^{-1}): the unitary standard concentration of the adsorbate MW (g mol^{-1}): molecular weight of the adsorption K_L (L mg^{-1}): Langmuir isotherm constant γ: (dimensionless) the coefficient of activity
$\ln K_e^0 = \frac{\Delta S^0}{R} - \frac{\Delta H^0}{R} \cdot \frac{1}{T}$(8)	ΔS^0 (kJ mol^{-1} K^{-1}): entropy change ΔH^0 (kJ mol^{-1}): enthalpy change T (K): temperature
$\Delta G^0 = \Delta H^0 - T \cdot \Delta S^0$(9)	ΔG^0 (kJ mol^{-1}): Gibbs free energy
PFO : $q_t = q_{e,cal.}(1 - e^{-k_1 t})$(10)	k_1 (min^{-1}): the rate constant of PFO kinetic model $q_{e,cal.}$ (mg g^{-1}): calculated equilibrium adsorption capacity
PSO : $q_e = \frac{q_{e,cal.}^2 \cdot k_2 \cdot t}{1+(q_{e,cal.} \cdot k_2 \cdot t)}$(11)	k_2 (g mg^{-1} min^{-1}): the rate constant of PSO kinetic mode h (mg g^{-1} min^{-1}) = $q_{e,cal.}^2 \cdot k_2$: the initial adsorption rate t (min): time
Elovich : $\frac{1}{\beta}\ln(\alpha \cdot \beta) + \frac{1}{\beta}\ln t$(12)	α (mg g^{-1} min^{-1}): the initial adsorption rate β (g mg^{-1}): a parameter related to the activation energy for chemisorption and extent of surface coverage

at specific times (t = 1, 3, 5, 10, 15, 30, 60, 120 min) and measured immediately afterward.

3. Results and discussion

3.1. Synthesis of the samples

$Ni_{50}Co_{50}$-LDH/UiO-66-NH_2 NC was synthesized by the *in situ* growth of UiO-66-NH_2 MOF nanocrystals on the surface of ultrathin nanosheets of functionalized $Ni_{50}Co_{50}$-LDH. UiO-66-NH_2 MOF was chosen because this MOF possesses free amine functional groups in its linker that can act as adsorption sites for the capture of heavy metals and, more importantly, this MOF shows good water and organic solvent resistance. $Ni_{50}Co_{50}$-LDH was chosen because it can be synthesized by a facile, large-scale, and environmentally friendly synthetic protocol in which no toxic organic solvents are used. Due to its extended 2D-ultrathin nanosheets, $Ni_{50}Co_{50}$-LDH can be a potential substrate to covalently anchor MOF nanocrystals. However, it is worth pointing out that before the *in situ* growth of MOF nanocrystals, in order to establish a strong chemical bond between LDH nanosheets and MOF nanocrystals, it is necessary to modify the surface of the LDH with a suitable silane coupling agent. Herein, we have functionalized $Ni_{50}Co_{50}$-LDH with CPTMS prior to the *in situ* growth of UiO-66-NH_2 nanocrystals (Fig. 1). Methoxy groups of CPTMS molecules can easily react with surface hydroxyl groups of LDH, and a number of carboxylic groups of MOF linkers (H_2N-H_2BDC) can form chemical bonds with carbon attached to chlorine atoms in CPTMS to form ester bonds (Fig. 1). This synthetic approach, in addition to establishing a strong chemical bond between the composite components (LDH and MOF), also results in a uniform distribution of MOF nanocrystals throughout $Ni_{50}Co_{50}$-LDH nanosheets, and accordingly the formation of a homogeneous composite structure. $Ni_{50}Co_{50}$-LDH/UiO-66-NH_2 NC decorated with abundant amine groups in its structure could be a potential adsorbent for capturing cationic heavy metals.

3.2. Characterization of the samples

The powder XRD patterns obtained for the samples are shown in Fig. 2 and demonstrate that the synthesized samples are indeed crystalline. $Ni_{50}Co_{50}$-LDH revealed characteristic X-ray diffraction peaks centered at 11.7, 21.7, 34.2, and 60.7, and $Ni_{50}Co_{50}$-LDH-Cl revealed peaks centered at 10.5, 20.5, 34.4, and 60.5 which are related to 2θ = (0 0 3), (0 0 6), (0 1 2), and (1 1 0) planes of nickel cobalt carbonate hydroxide hydrate (JCPDS 33–0429) which are in close agreement with previously reported results (Soltani et al., 2018; Soltani et al., 2020; Li et al., 2016). These XRD results clearly exhibited that both $Ni_{50}Co_{50}$-LDH and $Ni_{50}Co_{50}$-LDH-Cl possess a low degree of crystallinity and surface modification has no significant effect on the degree of crystallinity. For the UiO-66-NH_2 sample, it can be observed that the XRD peaks are consistent with those previously reported (Kandiah et al., 2010; Decoste et al.,

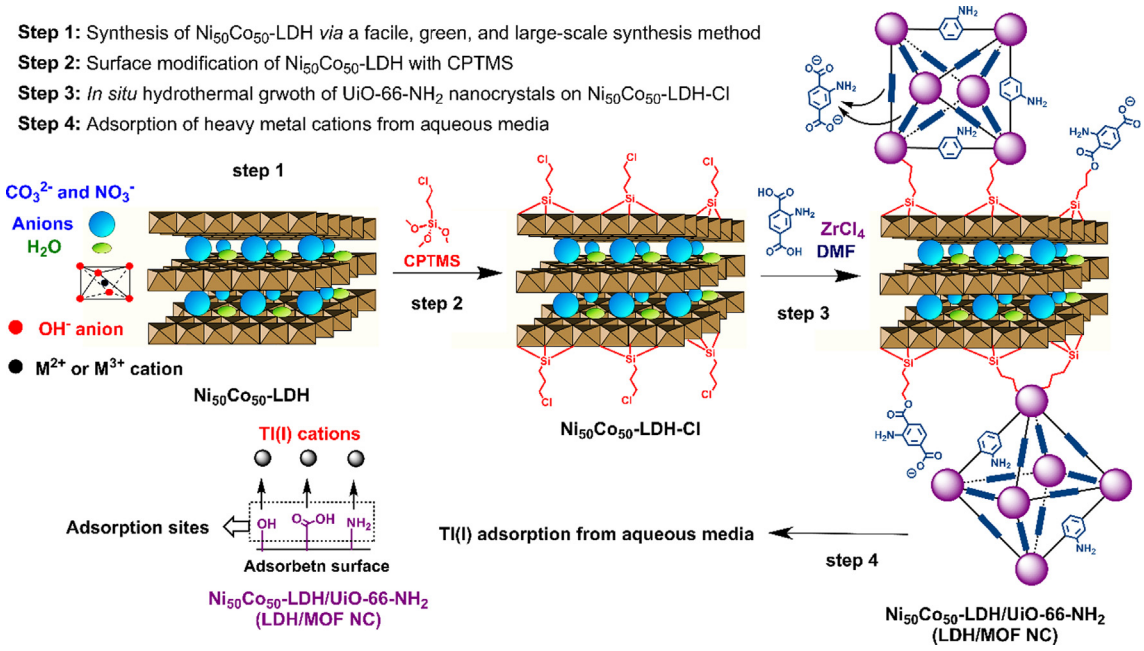

Fig. 1 The overall synthesis procedure of the $Ni_{50}Co_{50}$-LDH/UiO-66-NH_2 NC for the adsorption of Tl(I) from aqueous medium.

2013; Cavka et al., 2008). The two featured intensive peaks at $2\theta = 7.3°$ and 8.55° are attributed to the (111) and the (200) crystal planes, respectively. Also, less prominent peaks were observed at 26°, 30.8°, 43.8°, 50.5°, and 57.5°. The XRD pattern of $Ni_{50}Co_{50}$-LDH/UiO-66-NH_2 NC exhibited two featured diffraction peaks at $2\theta = 7.4°$ and 8.6°, which could be related to (111) and (002) planes of UiO-66-NH_2, demonstrating that MOF nanocrystals are grown on the $Ni_{50}Co_{50}$-LDH-Cl sheets.

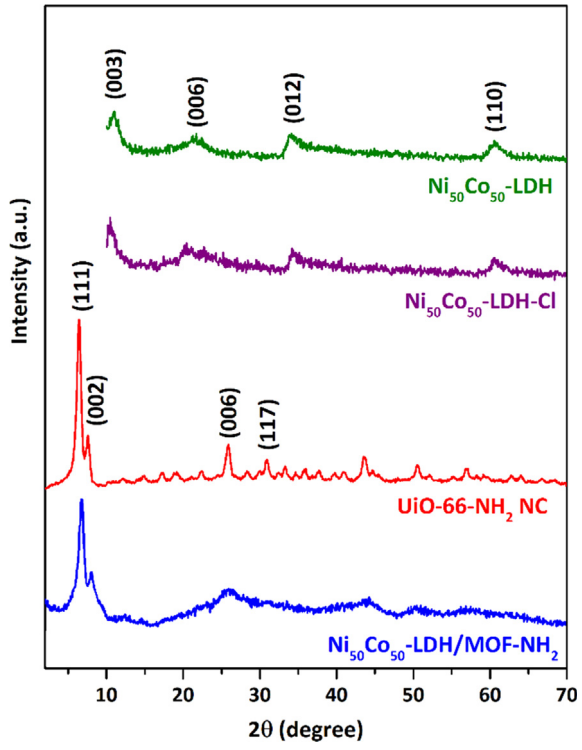

Fig. 2 Powder XRD patterns of the samples.

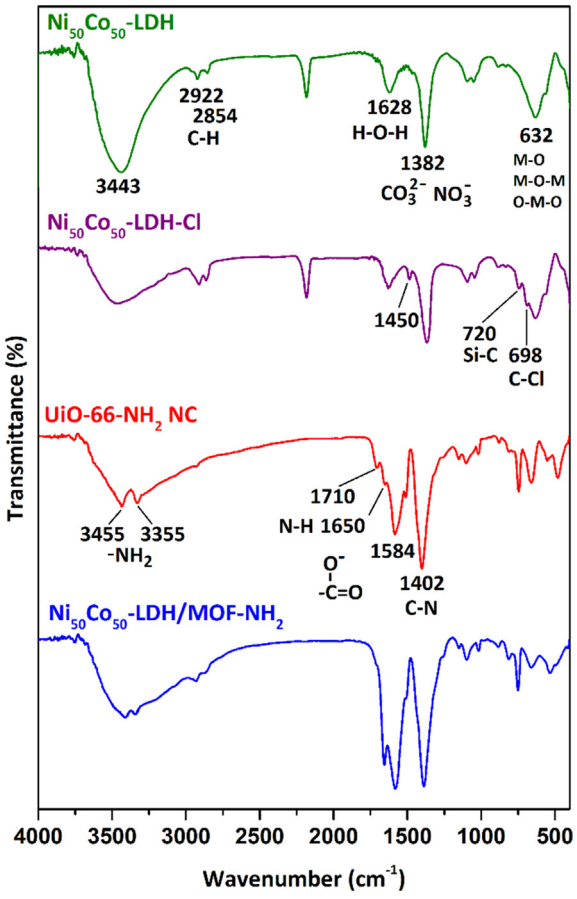

Fig. 3 FTIR spectra of the samples.

FTIR spectra of the prepared specimens are illustrated in Fig. 3. Both $Ni_{50}Co_{50}$-LDH and $Ni_{50}Co_{50}$-LDH-Cl samples have similar FTIR bands at around 3443, 1628, 1382, and 632 cm^{-1} which are attributed to the O-H stretching vibration, bending mode of water, the vibration of interlayer anions ($CO_3^{2-}$and NO_3^-), and metal-oxide vibrations, respectively (Soltani et al., 2018; Soltani et al., 2020). After surface modification of $Ni_{50}Co_{50}$-LDH with CPTMS new absorption bands appeared at 1450, 720, and 698 cm^{-1} which are due to C–H bending mode, Si–C stretching vibration, and C–Cl stretching vibration, respectively. The appearance of these absorption bands, along with a significant reduction in the intensity of the absorption band at 3443 cm^{-1} is indicative of the successful grafting of CPTMS on the surface of $Ni_{50}Co_{50}$-LDH. For UiO-66-NH_2, the absorption bands at 1402 and 1650 cm^{-1} is attributed to the C-N stretching mode and N–H scissoring

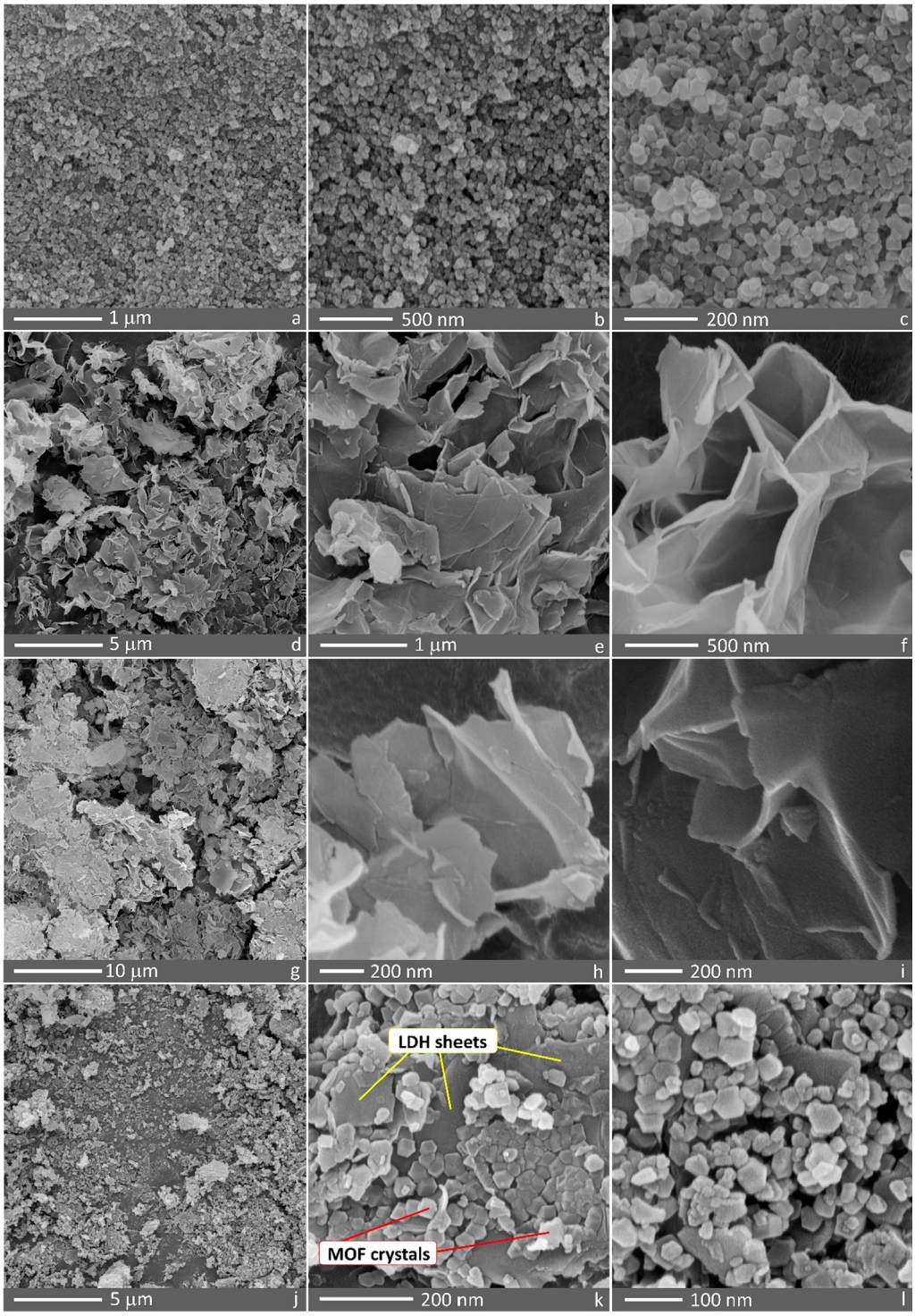

Fig. 4 FESEM images of (a-c) UiO-66-NH_2, (d-f) $Ni_{50}Co_{50}$-LDH, (g-i) $Ni_{50}Co_{50}$-LDH-Cl, and (j-l) $Ni_{50}Co_{50}$-LDH/UiO-66-NH_2 NC.

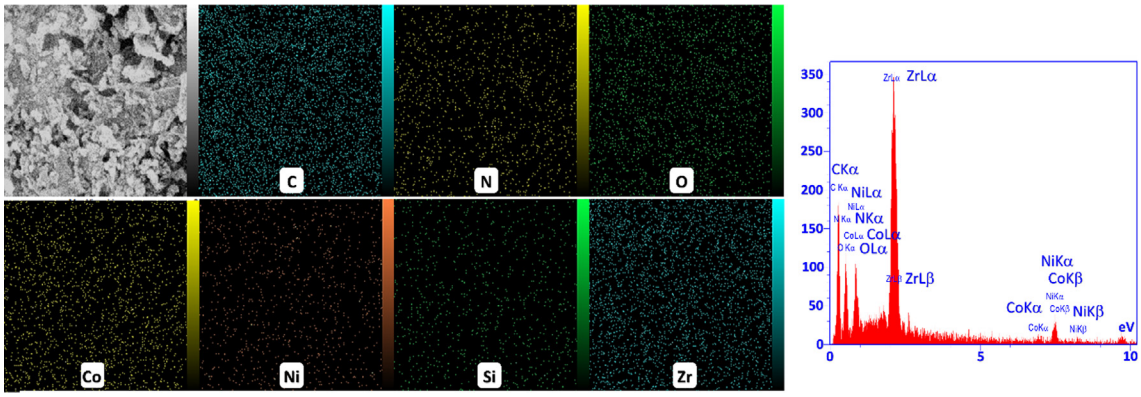

Fig. 5 Elemental mapping images for C, N, O, Co, Ni, Si, and Zr and the EDS spectrum of the $Ni_{50}Co_{50}$-LDH/UiO-66-NH_2 NC.

vibration in aromatic amines. The absorption bands at 1584 and 1710 cm^{-1} are attributed to the symmetric and asymmetric modes of Zr-bound carboxylate. Also, the absorption bands at 3455 and 3384 cm^{-1} represent, respectively, the symmetric and asymmetric N-H stretching vibration. After the *in situ* growth of MOF nanocrystals on the LDH surface, characteristic absorption bands related to both UiO-66-NH_2 and modified $Ni_{50}Co_{50}$-LDH are observed in the FTIR spectrum of Ni_{50}-Co_{50}-LDH/UiO-66-NH_2 NC, indicating the simultaneous presence of both structures in the nanocomposite.

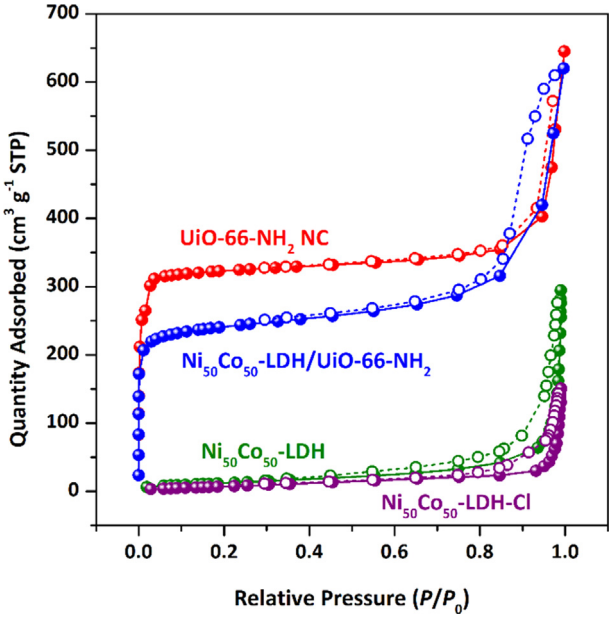

Fig. 6 N_2 adsorption–desorption isotherms of the samples at 77 K.

FESEM images of the samples are shown in Fig. 4. It can be seen that polygonal nanocrystals of UiO-66-NH_2 possess a uniform size distribution (Fig. 4a-c). Ultrathin nanosheets of $Ni_{50}Co_{50}$-LDH can be clearly observed in Fig. 4d-f. After surface modification of $Ni_{50}Co_{50}$-LDH with CPTMS, no significant difference was observed, indicating that surface modification has no significant effect on the surface morphology of the LDH nanosheets (Fig. 4g-i). Fig. 4j-l reveal the simultaneous presence of both structural components: UiO-66-NH_2 MOF crystals and $Ni_{50}Co_{50}$-LDH sheets are clearly visible in the structure of the $Ni_{50}Co_{50}$-LDH/UiO-66-NH_2 NC, indicating the successful synthesis of $Ni_{50}Co_{50}$-LDH/UiO-66-NH_2 NC by the *in situ* growing method. Interestingly, compared to previous works (Yang et al., 2017; Hu et al., 2018), the simultaneous presence of both MOF crystals (with well-dispersed nanoparticles) and LDH sheets in the nanocomposite structure is well visible, which is probably due to 1) the chemical surface modification of LDH, 2) synthesis method, and 3) the selection of suitable MOF and LDH for the nanocomposite formation.

Fig. 5 shows the EDS mapping images of $Ni_{50}Co_{50}$-LDH/UiO-66-NH_2 NC. These images demonstrated that structural elements of C, N, O, Co, Ni, Si, and Zr were uniformly distributed on the composite structure. Also, the EDS spectrum obtained from the $Ni_{50}Co_{50}$-LDH/UiO-66-NH_2 NC shows the peaks corresponding to all the aforementioned elements.

The N_2 adsorption–desorption isotherm profiles of the samples are revealed in Fig. 6 and their textural properties are given in Table 2. $Ni_{50}Co_{50}$-LDH and $Ni_{50}Co_{50}$-LDH-Cl show a characteristic type III isotherm with an H1 hysteresis loop,

Table 2 The textural properties of the samples (V_{pore}: total pore volume; V_{micro}: microporous volume; D: pore diameter calculated by NLDFT).

Samples	Surface area (m^2 g^{-1})			Pore volume (V, cm^3 g^{-1})		
	BET	Langmuir	t-plot	V_{pore}	V_{micro}	D (nm)
Ni_{50}-Co_{50} LDH	48	45	32	0.459	0.221	3.2
Ni_{50}-Co_{50} LDH-Cl	31	29	20	0.232	0.108	2.4
UiO-66-NH_2	1223	1250	1218	0.456	0.444	1.2
Ni_{50}-Co_{50} LDH/UiO-66-NH_2	907	916	554	0.909	0.111	2.1

indicating the existence of mesopores and macropores, which is due to gaps and large space between the adjacent interlayers of overlapping ultrathin nanosheets (Soltani et al., 2020; Li et al., 2016). After surface modification, the pore volume and surface area decreased slightly which is a common phenomenon during the surface modification with silane coupling agents *via* the post-modification method. Type I shape for UiO-66-NH_2 indicates that MOF nanocrystals possess microporous features with a pore diameter (D) of 1.2 nm. The shape of the isotherm for $Ni_{50}Co_{50}$-LDH/UiO-66-NH_2 NC is the same as that of UiO-66-NH_2 (Type I), except that the hysteresis loop in the UiO-66-NH_2 sample is wider, indicating the presence of larger pores (mesopores). The origin of these mesopores located in the composite structure is the existence of the LDH component in the composite structure. Compared to UiO-66-NH_2, a decrease in surface area and pore volume was observed for $Ni_{50}Co_{50}$-LDH/UiO-66-NH_2 NC which was predictable. The surface area of $Ni_{50}Co_{50}$-LDH, $Ni_{50}Co_{50}$-LDH-Cl, UiO-66-NH_2, $Ni_{50}Co_{50}$-LDH/UiO-66-NH_2 NC were found to be 48, 31, 1223, and 907 $m^2\ g^{-1}$ according to the BET equation. The microporous surface area calculated using the t-plot method was 32, 20, 1218, and 554 $m^2\ g^{-1}$ for $Ni_{50}Co_{50}$-LDH, $Ni_{50}Co_{50}$-LDH-Cl, UiO-66-NH_2, $Ni_{50}Co_{50}$-LDH/UiO-66-NH_2 NC, respectively. The large surface area and a high degree of porosity with a bimodal micro/mesoporosity, as well as amine-decorated pores, make $Ni_{50}Co_{50}$-LDH/UiO-66-NH_2 material a potential adsorbent for removal of cationic heavy metals.

3.3. Adsorption studies

3.3.1. The effect of pH and adsorbent dose

Solution pH is an important parameter in adsorption because it affects the surface charge of adsorbents and the chemistry of metal solutions (Glocheux et al., 2014). As shown in Fig. 7, the removal percentage of Tl(I) rises with increasing pH until it reaches a constant value in the range between 6.5 and 7.5 and then starts to decrease gradually from 7.5 to 8.5. This is a common adsorption behavior in many metal adsorption processes by adsorbents possessing functional groups like hydroxyl, amines, thiols, and ketones, known as the increasing-maximum-decreasing (IMD) pattern. According to the IMD model proposed by Soltani and co-workers (Soltani et al., 2020; Soltani et al., 2021; Soltani et al., 2019), in an acidic medium, the adsorption quantity of target adsorbate is low because of the competition between metal cations and H_3O^+ cations for interaction with surface functional groups of adsorbents. By enhancing the pH of solution and reducing competition, the adsorption is increased to reach its highest level. As shown in Fig. 7, with an increase in the adsorbent dose from 0.001 g to 0.002 g the removal percentage of Tl(I) cations increased considerably, but with an increase to 0.005 g, there was no significant increase in its removal percentage. For an adsorbent dose of 0.002 g and the pH range of 6.5–7.5, the removal percentage obtained was $\geq$ 98%. Accordingly, pH 7.0 and an adsorbent dose of 0.002 g were selected as optimal conditions for further adsorption investigations.

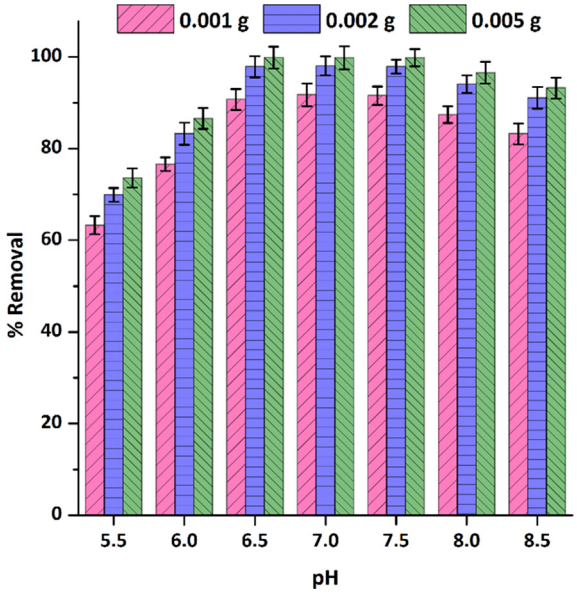

Fig. 7 The effect of pH and adsorbent dose on Tl(I) adsorption by $Ni_{50}Co_{50}$-LDH/UiO-66-NH_2 NC (pH = 5.5–8.5, C_i = 30 mg L^{-1}, V = 30 mL, W = 0.001–0.005 g, T = 293 K, shaking speed = 180 rpm).

3.3.2. The isotherm and thermodynamic studies (effect of initial concentration and temperature)

The simultaneous influence of initial Tl(I) concentration and solution temperature on the adsorption process were studied. As shown in Fig. 8a, for all three temperatures (293, 303, and 313 K), with increasing Tl(I) concentration the adsorption capacity goes up sharply until it is almost fixed at a point ($q_{m,exp.}$) and the adsorption reaches the equilibrium state. In order to gain a better understanding of the equilibrium adsorption isotherms, three non-linear isotherm models, namely Langmuir, Freundlich, and Redlich-Peterson (R-P) (Eqs. (4–6) in Table 1), were used to fit experimental adsorption equilibrium data. These adsorption isotherm curves, after non-linear fitting, are shown in Fig. 8a for three temperatures, and the corresponding parameters and R^2 values (adjusted R^2) are listed in Table 3. The adsorption isotherms of Tl(I) at all three temperatures present a good Langmuir fit ($R^2 \sim 0.94$–0.98) in comparison with Freundlich ($R^2 \sim 0.88$), implying that the active sites (adsorption functional groups) were distributed homogenously on the $Ni_{50}Co_{50}$-LDH/UiO-66-NH_2 NC, and that monolayer adsorption occurred on a limited number of identical and equivalent localized sites (Soltani et al., 2020). The calculated maximum adsorption capacity of Tl(I) reached 601.3 mg g^{-1}, surpassing the largest reported adsorption capacities in Table 4. Also, the closeness of the calculated maximum adsorption capacities ($q_{m,cal.}$ = 601.3, 626.5, and 650.7 mg g^{-1} at 293, 303, and 313 K, respectively) with their experimental values ($q_{m,exp..}$ = 600.0, 626.3, 649.5 mg g^{-1} at 293, 303, and 313 K, respectively) indicates a very good agreement of the Langmuir isotherm model with experimental data.

R-P isotherm is a three-parameter model that combines features of both Freundlich and Langmuir isotherms in one equation (Redlich and Peterson, 1959). It can be applied to determine whether the adsorption isotherm follows Langmuir or Freundlich's characteristics. In this equation (Eq. (6)), when g = 1 it becomes the Langmuir equation and when g = 0 it approaches the Freundlich equation (K_{R-P} and $\alpha_{R-P} \gg 1$).

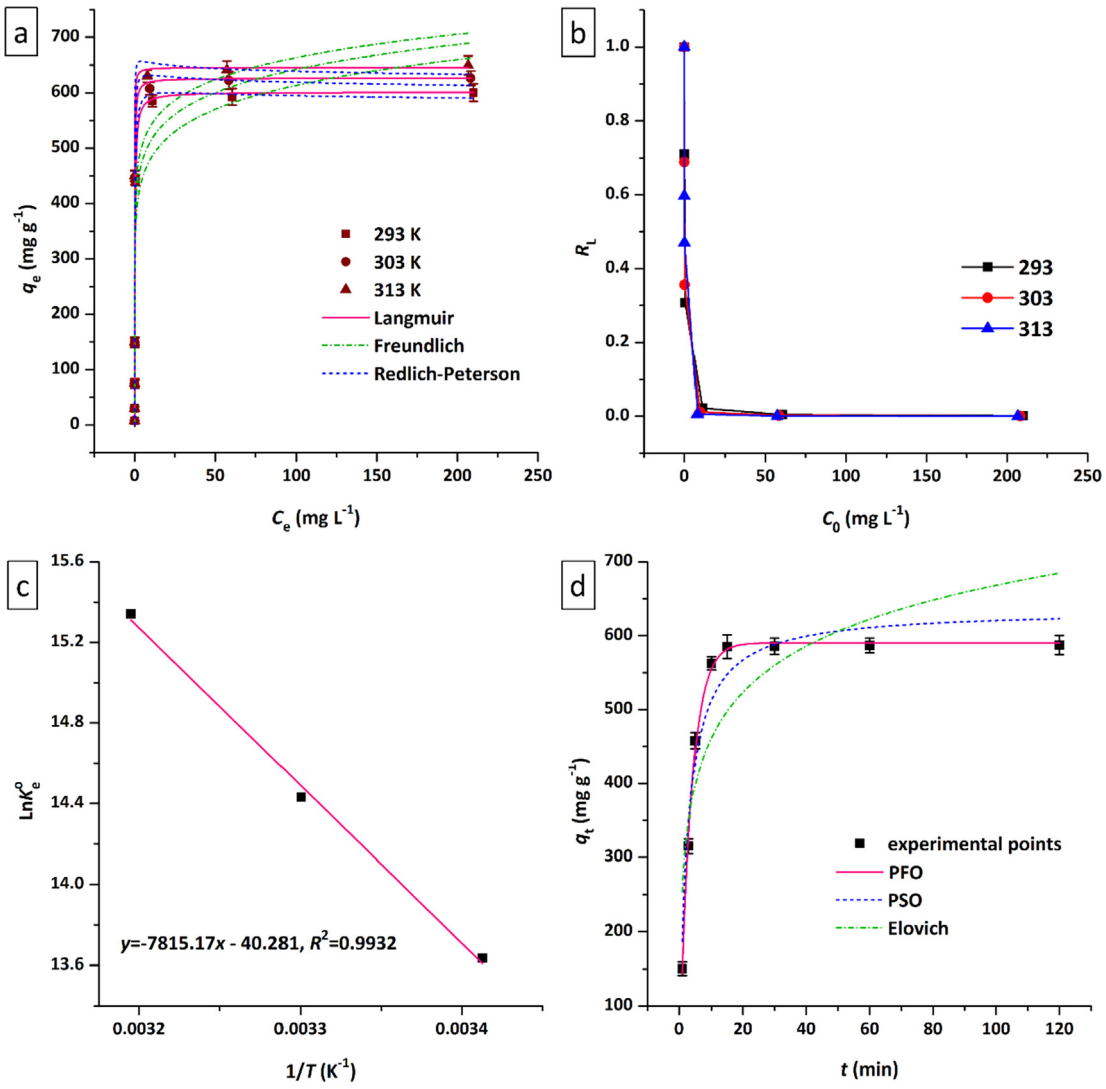

Fig. 8 Diagrams related to (a) the effect of initial concentration of Tl(I) on the adsorption capacity and isotherm curves, (b) R_L values, and (c) corresponding thermodynamic curve for adsorption of Tl(I) on $Ni_{50}Co_{50}$-LDH/UiO-66-NH_2 NC (pH = 7.0, V = 30 mL, W = 0.002 g, t = 120 min, shaking speed = 180 rpm). (d) The effect of time on the adsorption of Tl(I) by $Ni_{50}Co_{50}$-LDH/UiO-66-NH_2 NC and corresponding kinetic curves (pH = 7.0, C_i = 50 mg L^{-1}, V = 30 mL, W = 0.002 g, T = 293 K, shaking speed = 180 rpm).

Table 3 Isotherm parameters for adsorption of Tl(I) on $Ni_{50}Co_{50}$-LDH/UiO-66-NH_2 NC at 293–313 K.

		Values		
Isotherms	Parameters	293 K	303 K	313 K
	$q_{m,exp.}$(mg g^{-1})	600.0	626.3	649.5
Langmuir	$q_{m,cal.}$(mg g^{-1})	601.3	626.5	650.7
	K_L (L mg^{-1})	4.087	9.051	22.512
	R^2	0.9817	0.9775	0.9401
Freundlich	K_F (mg g^{-1})(L g^{-1})^n	377.3	409.6	440.7
	n (-)	9.483	10.247	11.259
	R^2	0.8854	0.8862	0.8775
R-P	K_{R-P} (L g^{-1})	2287.5	5271.2	13658.0
	α_{R-P} (L mg^{-1})	3.626	8.006	20.195
	g (-)	0.998	0.992	0.989
	R^2	0.9788	0.9740	0.9289

Table 4 Maximum adsorption capacity of various adsorbents toward Tl(I).

Adsorbents	Groups	Year	$q_{m,cal.}$(mg g^{-1})	Conditions			Ref
				pH	t(min/h)	T(℃)	
LDH/MOF NC	Soltani et al.	2020	601.3	6.5	20	20	This work
TMS-SMSs	Soltani et al.	2019	452.8	6.0	50 min	25	(Soltani et al., 2019)
titanium peroxide	Zhang et al.	2018	412.0	7.0	4 h	25	(Zhang et al., 2018)
MnO_2@ pyrite cinder	Li et al.	2018	290.7	12.0	30 min	25	(Li et al., 2018)
Fe-Mn binary oxides	Li et al.	2017	236.4	10.0	24 h	35	(Li et al., 2017)
HMO	Wan et al.	2014	352.9	5.0	40 min	15	(Wan et al., 2014)
Eucalyptus leaves	Dashti et al.	2013	80.7	8.5	30 min	25	(Dashti Khavidaki and Aghaie, 2013)
FC-Cu-EDA-SAMMS	Sangvanich et al.	2010	28.3	7.8	NR	RT	(Sangvanich et al., 2010)
nano-Al_2O_3	Zhang et al.	2008	6.3	4.5	10 min	40	(Zhang et al., 2008)

LDH/MOF NC: $Ni_{50}Co_{50}$-LDH/UiO-66-NH_2 nanocomposite; TMS-SMSs: thiol-modified mesoporous silica submicrospheres; HMO: amorphous hydrous manganese dioxide; FC-Cu-EDA-SAMMS: copper(II) ferrocyanide on mesoporous silica.

As shown in Table 3, the values of g parameter for adsorption of Tl(I) on the adsorbent at all three temperatures were very close to unity, implying that the Langmuir model showed a better fit than the Freundlich.

According to Hall et al. (Hall et al., 1966), an essential characteristic of the Langmuir equation could be illustrated in terms of separation factor (R_L, Table 1) which is a unitless equilibrium factor and proposes the adsorption nature and possibility of the adsorption phenomenon: $R_L > 1$, unfavorable;$R_L = 1$, linear; $0 < R_L < 1$, favorable; $R_L = 0$, irreversible. As shown in Fig. 8b, for the adsorption of Tl(I) on the Ni_{50}-Co_{50}-LDH/UiO-66-NH_2 NC, the R_L values obtained are between zero and one, demonstrating a favorable adsorption process.

The influence of solution temperature on the adsorption of Tl(I) cations by $Ni_{50}Co_{50}$-LDH/UiO-66-NH_2 NC was studied. As shown in Fig. 8a, the adsorption capacity increases with increasing temperature. For example, with increasing temperature from 293 K to 303 K and 313 K, the adsorption capacity reaches 626.3 and 649.5 mg g^{-1}, respectively (Table 3). In the Langmuir equation, K_L constant indicates the affinity between an adsorbent and a target adsorbate. The higher the value of this parameter, the greater the affinity to adsorb the target species. As the solution temperature rises, the value of K_L parameter and accordingly the adsorption affinity of $Ni_{50}Co_{50}$-LDH/UiO-66-NH_2 NC toward Tl(I) cations continually increases. This trend is in close agreement with the changes in the uptake capacities of Tl(I) with temperature, as can be seen in Fig. 8a and Table 3. In order to gain more insight into the temperature-dependent behavior of Tl(I) adsorption on the adsorbent and assess the feasibility of the adsorption procedure thermodynamic studies were conducted. For this purpose, important thermodynamic parameters such as ΔH^0, ΔS^0, and ΔG^0 were obtained from the equations 7–9 given in Table 1.

It is reported that the right method for estimating K_e^0 values in the adsorption procedure is to determine the best fitted-nonlinear isotherm (generally the Langmuir isotherm) at several temperatures (Lima et al., 273 (2019)). Furthermore, it is assumed that the concentration of target adsorbate in an aqueous medium is very low to presume that the activity coefficient (γ) is unitary. So, in these circumstances, for each Langmuir isotherm at a certain temperature (Fig. 8a), a value of K_L is determined, resulting in a value of K_e^0 (Eq. (7)), which can be used to estimate the value of ΔH^0 and ΔS^0 (Eq. (8)), and, consequently, ΔG^0 values (Eq. (9)). The estimated values of ΔH^0, ΔS^0, and ΔG^0 are given in Table 5 and the corresponding thermodynamic curve is shown in Fig. 8c.

According to the literature, in an adsorption process, the magnitude of ΔG^0 and ΔH^0 can suggest the kind of interactions between the adsorbent and adsorbate: $-20 < \Delta G^0 < 0$ kJ mol^{-1}, physical adsorption; $-400 < \Delta G^0 < -80$ kJ mol^{-1}, chemical adsorption; $4 < \Delta H^0 < 10$ kJ mol^{-1}, van der Waals forces; $2 < \Delta H^0 < 29$ kJ mol^{-1}, dipole–dipole interactions; $2 < \Delta H^0 < 40$ kJ mol^{-1}, hydrogen bonding forces; $\Delta H^0 \approx 40$ kJ mol^{-1}, exchange of dentate; $\Delta H^0 > 60$ kJ mol^{-1}, chemical bonding forces (Soltani et al., 2020; Zhou et al., 2014). The obtained ΔH^0 and ΔS^0 values for adsorption of Tl(I) cations on the adsorbent are + 64.979 kJ mol^{-1} and 0.335 kJ mol^{-1} K^{-1}, respectively, indicating that the adsorption process is endothermic with an increase in randomness at the solid/liquid interface with rising temperature. Furthermore, ΔG^0 became more negative with an increase in temperature, indicating a more efficient Tl(I) adsorption onto $Ni_{50}Co_{50}$-LDH/UiO-66-NH_2 NC at a higher temperature. The values of ΔG^0 and ΔH^0 demonstrate that the adsorption of Tl(I) on the $Ni_{50}Co_{50}$-LDH/UiO-66-NH_2 NC is more chemical than physical.

Table 5 Thermodynamic parameters for adsorption of Tl(I) on $Ni_{50}Co_{50}$-LDH/UiO-66-NH_2 NC.

ΔH^0 (kJ mol^{-1})	ΔS^0 (kJ mol^{-1} K^{-1})	ΔG^0 (kJ mol^{-1})		
		293	303	313
64.979	0.335	−33.176	−36.526	−39.876

Table 6 Kinetic parameter values for adsorption of Tl(I) on $Ni_{50}Co_{50}$-LDH/UiO-66-NH_2 NC at 293 K.

Kinetics	Parameters	Values
	$q_{e,m.}$ (mg g^{-1})	587.5
PFO	$q_{e,cal.}$ (mg g^{-1})	590.2
	k_1 (min^{-1})	0.2798
	R^2	0.9955
PSO	$q_{e,cal.}$ (mg g^{-1})	635.4
	k_2 (g mg^{-1} min^{-1})	6.54×10^{-4}
	h (mg g^{-1} min^{-1})	264.0
	R^2	0.9420
Elovich	α (mg g^{-1} min^{-1})	1501.9
	β (g mg^{-1})	0.0111
	R^2	0.7218

3.3.3. The kinetic studies (effect of contact time)

The effect of contact time on the adsorption of Tl(I) onto Ni_{50}-Co_{50}-LDH/UiO-66-NH_2 NC was studied. As shown in Fig. 8d, with increasing time, the amount of adsorption capacity increases continuously with a steep slope until it reaches a constant value in about 15 min. This observation reveals that the adsorption rate of Tl(I) by the adsorbent is high, which can be attributed to the presence of abundant active adsorption sites (amine groups and aromatic rings) in the adsorbent structure as well as the high surface area of the adsorbent.

In order to gain better insight into the kinetics of the adsorption, non-linear forms of three kinetic models, namely pseudo-first-order (PFO), pseudo-second-order (PSO), and Elovich, were used and fitted to the experimental data. Table 1 lists these kinetic equations, and the corresponding kinetic parameter values after non-linear fitting are tabulated in Table 6.

The kinetic results are closely fitted by the PFO kinetic equation, with a high R^2 value ($R^2 = 0.9955$). In addition, compared with the PSO model, the calculated equilibrium adsorption capacity ($q_{e,cal.}$) estimated from the PFO model ($q_{e,cal.} = 590.2$) is much closer to the experimental equilibrium adsorption capacity ($q_{e,exp.} = 587.5$).

4. Conclusion

$Ni_{50}Co_{50}$-LDH/UiO-66-NH_2 NC was synthesized through a facile ultrasonic-assisted hydrothermal method. UiO-66-NH_2 MOF nanocrystals were *in situ* grown on the surface of 2D-ultrathin functionalized $Ni_{50}Co_{50}$-LDH nanosheets. Using this method, a uniform nanocomposite architecture was obtained by uniformly distributing MOF nanocrystals on the $Ni_{50}Co_{50}$-LDH. XRD, FTIR, FESEM/EDS/Mapping, and N_2 adsorption–desorption analyses were performed to characterize the physicochemical properties of the synthesized samples. The $Ni_{50}Co_{50}$-LDH/UiO-66-NH_2 NC has remarkable features of potential nanoadsorbent, including chemical functionality, high surface area (907 m^2 g^{-1}), large pore volume (0.91 cm^3 g^{-1}), and bimodal micro-mesoporous architecture. Therefore, $Ni_{50}Co_{50}$-LDH/UiO-66-NH_2 NC was used as an adsorbent for the removal of toxic Tl(I) from water. Different important parameters affecting the adsorption process were systematically studied and isotherm, thermodynamic, and kinetic investigations were conducted to gain a better understanding of the adsorption behavior and plausible mechanisms involved in the adsorption process. After non-linear fitting analysis, it was found that the Langmuir isotherm presents a better fit to the equilibrium data, and the maximum Langmuir adsorption capacity was found to be 601.3 mg g^{-1} (conditions: pH = 7.0, adsorbent dose = 0.002 g, solution volume = 30 mL, time = 15 min, temperature = 293 K, shaking speed = 180 rpm) surpassing the best previously reported adsorption capacities for Tl(I) by various adsorbents. Thermodynamic parameters were estimated ($\Delta H^0 = +64.979$ kJ mol^{-1}, $\Delta S^0 = +0.335$ kJ mol^{-1} K^{-1}, $\Delta G^0 = -33.176$ to -39.876 kJ mol^{-1}) and it was found that the adsorption of Tl(I) by the Ni_{50}-Co_{50}-LDH/UiO-66-NH_2 NC is endothermic and spontaneous and the adsorption nature is more chemical than physical.

CRediT authorship contribution statement

Roozbeh Soltani: Conceptualization, Methodology, Software, Validation, Formal analysis, Investigation, Writing - original draft, Writing - review & editing, Project administration. **Rasool Pelalak:** Software, Validation. **Mahboubeh Pishnamazi:** Software, Validation, Investigation. **Azam Marjani:** Resources, Supervision. **Shaheen M. Sarkar:** Validation, Investigation, Writing - review & editing. **Ahmad B. Albadarin:** Investigation, Writing - review & editing. **Saeed Shirazian:** Resources, Validation, Investigation, Supervision, Funding acquisition.

Declaration of Competing Interest

The authors declared that there is no conflict of interest.

Acknowledgments

Saeed Shirazian acknowledges the supports by the Government of the Russian Federation (Act 211, contract 02. A03.21.0011) and by the Ministry of Science and Higher Education of Russia (grant FENU- 2020-0019).

References

Peter, A.L.J., Viraraghavan, T., 2005. Thallium: A review of public health and environmental concerns. Environ. Int. 31, 493–501. https://doi.org/10.1016/j.envint.2004.09.003.

Cvjetko, P., Cvjetko, I., Pavlica, M., 2010. Thallium toxicity in humans. Arh. Hig. Rada Toksikol. 61, 111–119. https://doi.org/10.2478/10004-1254-61-2010-1976.

Sangvanich, T., Sukwarotwat, V., Wiacek, R.J., Grudzien, R.M., Fryxell, G.E., Addleman, R.S., Timchalk, C., Yantasee, W., 2010. Selective capture of cesium and thallium from natural waters and simulated wastes with copper ferrocyanide functionalized mesoporous silica. J. Hazard. Mater. 182, 225–231. https://doi.org/10.1016/j.jhazmat.2010.06.019.

Dashti Khavidaki, H., Aghaie, H., 2013. Adsorption of Thallium(I) Ions Using Eucalyptus Leaves Powder. Clean - Soil, Air, Water. 41, 673–679. https://doi.org/10.1002/clen.201200378.

Wan, S., Ma, M., Lv, L., Qian, L., Xu, S., Xue, Y., Ma, Z., 2014. Selective capture of thallium(I) ion from aqueous solutions by amorphous hydrous manganese dioxide. Chem. Eng. J. 239, 200–206. https://doi.org/10.1016/j.cej.2013.11.010.

Twidwell, L., Williams-Beam, C., 2002. Potential technologies for removing thallium from mine and process wastewater: an annotation of the literature. Eur. J. Miner. Process. Environ. Prot. 2, 1–10.

Burakov, A.E., Galunin, E.V., Burakova, I.V., Kucherova, A.E., Agarwal, S., Tkachev, A.G., Gupta, V.K., 2018. Adsorption of heavy metals on conventional and nanostructured materials for wastewater treatment purposes: A review. Ecotoxicol. Environ. Saf. 148, 702–712. https://doi.org/10.1016/j.ecoenv.2017.11.034.

Carolin, C.F., Kumar, P.S., Saravanan, A., Joshiba, G.J., Naushad, M., 2017. Efficient techniques for the removal of toxic heavy metals from aquatic environment: A review. J. Environ. Chem. Eng. 5, 2782–2799. https://doi.org/10.1016/j.jece.2017.05.029.

Azimi, A., Azari, A., Rezakazemi, M., Ansarpour, M., 2017. Removal of Heavy Metals from Industrial Wastewaters: A Review. ChemBioEng Rev. 4, 37–59. https://doi.org/10.1002/cben.201600010.

Pelalak, R., Soltani, R., Heidari, Z., Malekshah, R.E., Aallaei, M., Marjani, A., Rezakazemi, M., Kurniawan, T.A., Shirazian, S., 2021. Molecular dynamics simulation of novel diamino-functionalized hollow mesosilica spheres for adsorption of dyes from synthetic wastewater. J. Mol. Liq. 322. https://doi.org/10.1016/j.molliq.2020.114812. 114812.

Marjani, A., Soltani, R., Pishnamazi, M., Rezakazemi, M., Shirazian, S., 2020. Functionalized pollen-like mesoporous silica for Cr(VI) removal. Microporous Mesoporous Mater. 310. https://doi.org/10.1016/j.micromeso.2020.110531. 110531.

Pelalak, R., Soltani, R., Heidari, Z., Malekshah, R.E., Aallaei, M., Marjani, A., Rezakazemi, M., Shirazian, S., 2021. Synthesis, molecular dynamics simulation and adsorption study of different pollutants on functionalized mesosilica. Sci. Rep. 11, 1–13. https://doi.org/10.1038/s41598-020-80566-w.

Soltani, R., Marjani, A., Hosseini, M., Shirazian, S., 2020. Mesostructured Hollow Siliceous Spheres for Adsorption of Dyes. Chem. Eng. Technol. 43, 392–402. https://doi.org/10.1002/ceat.201900470.

Soltani, R., Marjani, A., Hosseini, M., Shirazian, S., 2020. Synthesis and characterization of novel N-methylimidazolium-functionalized KCC-1: A highly efficient anion exchanger of hexavalent chromium. Chemosphere 239. https://doi.org/10.1016/j.chemosphere.2019.124735. 124735.

Soltani, R., Marjani, A., Soltani, R., Shirazian, S., 2020. Hierarchical multi-shell hollow micro–meso–macroporous silica for Cr(VI) adsorption. Sci. Rep. 10, 1–12. https://doi.org/10.1038/s41598-020-66540-6.

Yanyan, L., Kurniawan, T.A., Zhu, M., Ouyang, T., Avtar, R., Dzarfan Othman, M.H., Mohammad, B.T., Albadarin, A.B., 226 (2018). Removal of acetaminophen from synthetic wastewater in a fixed-bed column adsorption using low-cost coconut shell waste pretreated with NaOH, HNO3, ozone, and/or chitosan. J. Environ. Manage. 226, 365–376. https://doi.org/10.1016/j.jenvman.2018.08.032.

Albadarin, A.B., Solomon, S., Kurniawan, T.A., Mangwandi, C., Walker, G., 2017. Single, simultaneous and consecutive biosorption of Cr(VI) and Orange II onto chemically modified masau stones. J. Environ. Manage. 204, 365–374. https://doi.org/10.1016/j.jenvman.2017.08.042.

Soltani, R., Shahvar, A., Dinari, M., Saraji, M., 2018. Environmentally-friendly and ultrasonic-assisted preparation of two-dimensional ultrathin Ni/Co-NO_3 layered double hydroxide nanosheet for micro solid-phase extraction of phenolic acids from fruit juices. Ultrason. Sonochem. 40, 395–401. https://doi.org/10.1016/j.ultsonch.2017.07.031.

Zubair, M., Daud, M., McKay, G., Shehzad, F., Al-Harthi, M.A., 2017. Recent progress in layered double hydroxides (LDH)-containing hybrids as adsorbents for water remediation. Appl. Clay Sci. 143, 279–292. https://doi.org/10.1016/j.clay.2017.04.002.

Feng, M., Zhang, P., Zhou, H.C., Sharma, V.K., 2018. Water-stable metal-organic frameworks for aqueous removal of heavy metals and radionuclides: A review. Chemosphere 209, 783–800. https://doi.org/10.1016/j.chemosphere.2018.06.114.

Khan, N.A., Hasan, Z., Jhung, S.H., 2013. Adsorptive removal of hazardous materials using metal-organic frameworks (MOFs): A review. J. Hazard. Mater. 244–245, 444–456. https://doi.org/10.1016/j.jhazmat.2012.11.011.

Madden, D.G., Albadarin, A.B., O'Nolan, D., Cronin, P., Perry, J.J., Solomon, S., Curtin, T., Khraisheh, M., Zaworotko, M.J., Walker, G.M., 2020. Metal-Organic Material Polymer Coatings for Enhanced Gas Sorption Performance and Hydrolytic Stability under Humid Conditions. ACS Appl. Mater. Interfaces 12, 33759–33764. https://doi.org/10.1021/acsami.0c08078.

Li, N., Du, J., Wu, D., Liu, J., Li, N., Sun, Z., Li, G., Wu, Y., 2018. Recent advances in facile synthesis and applications of covalent organic framework materials as superior adsorbents in sample pretreatment. TrAC - Trends Anal. Chem. 108, 154–166. https://doi.org/10.1016/j.trac.2018.08.025.

Wang, J., Zhuang, S., 2019. Covalent organic frameworks (COFs) for environmental applications 213046 Coord. Chem. Rev. 400. https://doi.org/10.1016/j.ccr.2019.213046.

Heydari, M., Jafari, M.T., Saraji, M., Soltani, R., Dinari, M., 2021. Covalent triazine-based framework-grafted functionalized fibrous silica sphere as a solid-phase microextraction coating for simultaneous determination of fenthion and chlorpyrifos by ion mobility spectrometry. Microchim. Acta 188, 1–11. https://doi.org/10.1007/s00604-020-04685-x.

Soltani, R., Pishnamazi, M., Pelalak, R., Rezakazemi, M., Marjani, A., Dinari, M., Sarkar, S.M., Shirazian, S., 2020. Preparation of COOH-KCC-1/polyamide 6 composite by in situ ring-opening polymerization: synthesis, characterization, and Cd(II) adsorption study. J. Environ. Chem. Eng. https://doi.org/10.1016/j.jece.2020.104683. 104683.

Soltani, R., Marjani, A., Moguei, M.R.S., Rostami, B., Shirazian, S., 2019. Novel diamino-functionalized fibrous silica submicro-spheres with a bimodal-micro-mesoporous network: Ultrasonic-assisted fabrication, characterization, and their application for superior uptake of Congo red. J. Mol. Liq. 294. https://doi.org/10.1016/j.molliq.2019.111617. 111617.

Soltani, R., Marjani, A., Hosseini, M., Shirazian, S., 2020. Meso-architectured siliceous hollow quasi-capsule. J. Colloid Interface Sci. 570, 390–401. https://doi.org/10.1016/j.jcis.2020.03.003.

Gang, D., Uddin Ahmad, Z., Lian, Q., Yao, L., Zappi, M.E., 2021. A review of adsorptive remediation of environmental pollutants from aqueous phase by ordered mesoporous carbon 126286 Chem. Eng. J. 403. https://doi.org/10.1016/j.cej.2020.126286.

Lim, J.Y., Mubarak, N.M., Abdullah, E.C., Nizamuddin, S., Khalid, M., 2018. Inamuddin, Recent trends in the synthesis of graphene and graphene oxide based nanomaterials for removal of heavy metals—A review. J. Ind. Eng. Chem. 66, 29–44. https://doi.org/10.1016/j.jiec.2018.05.028.

Zhang, Q., Hou, Q., Huang, G., Fan, Q., 2020. Removal of heavy metals in aquatic environment by graphene oxide composites: a review. Environ. Sci. Pollut. Res. 27, 190–209. https://doi.org/10.1007/s11356-019-06683-w.

Zabihi, S., Jamshidian, S., Soltani, R., Pelalak, R., Heidari, Z., Marjani, A., Ghadiri, M., 2020. *In situ* polymerized FDU-12/PMMA and FDU-12/polyamide 6 nanocomposites for Cd(II) adsorption. Chem. Eng. Technol. https://doi.org/10.1002/ceat.202000298.

Zarei, F., Marjani, A., Soltani, R., 2019. Novel and green nanocomposite-based adsorbents from functionalised mesoporous KCC-1 and chitosan-oleic acid for adsorption of Pb(II). Eur. Polym. J. 119, 400–409. https://doi.org/10.1016/j.eurpolymj.2019.07.043.

Soltani, R., Marjani, A., Shirazian, S., 2020. A hierarchical LDH/MOF nanocomposite: Single, simultaneous and consecutive adsorption of a reactive dye and Cr(vi). Dalt. Trans. 49, 5323–5335. https://doi.org/10.1039/d0dt00680g.

Zhang, X., Shi, X., Chen, J., Yang, Y., Lu, G., 2019. The preparation of defective UiO-66 metal organic framework using MOF-5 as structural modifier with high sorption capacity for gaseous toluene. J. Environ. Chem. Eng. 7. https://doi.org/10.1016/j.jece.2019.103405. 103405.

Zhang, Z., Wang, S., Bao, M., Ren, J., Pei, S., Yu, S., Ke, J., 2019. Construction of ternary Ag/AgCl/NH_2-UiO-66 hybridized heterojunction for effective photocatalytic hexavalent chromium reduction. J. Colloid Interface Sci. 555, 342–351. https://doi.org/10.1016/j.jcis.2019.07.103.

Wang, S., Meng, F., Sun, X., Bao, M., Ren, J., Yu, S., Zhang, Z., Ke, J., Zeng, L., 2020. Bimetallic Fe/In metal-organic frameworks boosting charge transfer for enhancing pollutant degradation in wastewater. Appl. Surf. Sci. 528. https://doi.org/10.1016/j.apsusc.2020.147053. 147053.

Yang, Q., Vaesen, S., Ragon, F., Wiersum, A.D., Wu, D., Lago, A., Devic, T., Martineau, C., Taulelle, F., Llewellyn, P.L., Jobic, H., Zhong, C., Serre, C., De Weireld, G., Maurin, G., 2013. A water stable metal-organic framework with optimal features for CO_2 capture. Angew. Chemie - Int. Ed. 52, 10316–10320. https://doi.org/10.1002/anie.201302682.

Soltani, R., Pelalak, R., Pishnamazi, M., Marjani, A., Albadarin, A.B., Sarkar, S.M., Shirazian, S., 2021. A novel and facile green synthesis method to prepare LDH/MOF nanocomposite for removal of Cd (II) and Pb (II). Sci. Rep. 11, 1–15. https://doi.org/10.1038/s41598-021-81095-w.

Shi, X., Zhang, X., Bi, F., Zheng, Z., Sheng, L., Xu, J., Wang, Z., Yang, Y., 2020. Effective toluene adsorption over defective UiO-66-NH_2: An experimental and computational exploration. J. Mol. Liq. 316. https://doi.org/10.1016/j.molliq.2020.113812. 113812.

Yang, Y., Zheng, Z., Yang, M., Chen, J., Li, C., Zhang, C., Zhang, X., 2020. In-situ fabrication of a spherical-shaped Zn-Al hydrotalcite with BiOCl and study on its enhanced photocatalytic mechanism for perfluorooctanoic acid removal performed with a response surface methodology. J. Hazard. Mater. 399. https://doi.org/10.1016/j.jhazmat.2020.123070. 123070.

Yang, Y., Yang, M., Zheng, Z., Zhang, X., 2020. Highly effective adsorption removal of perfluorooctanoic acid (PFOA) from aqueous solution using calcined layer-like Mg-Al hydrotalcites nanosheets. Environ. Sci. Pollut. Res. 27, 13396–13408. https://doi.org/10.1007/s11356-020-07892-4.

Yang, Y., Yan, X., Hu, X., Feng, R., Zhou, M., 2017. In-situ growth of ZIF-8 on layered double hydroxide: Effect of Zn/Al molar ratios on their structural, morphological and adsorption properties. J. Colloid Interface Sci. 505, 206–212. https://doi.org/10.1016/j.jcis.2017.05.100.

Hu, M., Lou, H., Yan, X., Hu, X., Feng, R., Zhou, M., 2018. In-situ fabrication of ZIF-8 decorated layered double oxides for adsorption and photocatalytic degradation of methylene blue. Microporous Mesoporous Mater. 271, 68–72. https://doi.org/10.1016/j.micromeso.2018.05.048.

Kandiah, M., Nilsen, M.H., Usseglio, S., Jakobsen, S., Olsbye, U., Tilset, M., Larabi, C., Quadrelli, E.A., Bonino, F., Lillerud, K.P., 2010. Synthesis and stability of tagged UiO-66 Zr-MOFs. Chem. Mater. 22, 6632–6640. https://doi.org/10.1021/cm102601v.

Kumar, K.V., Sivanesan, S., 2006. Selection of optimum sorption kinetics: Comparison of linear and non-linear method. J. Hazard. Mater. 134, 277–279. https://doi.org/10.1016/j.jhazmat.2005.11.003.

Soltani, R., Marjani, A., Shirazian, S., 2019. Facile one-pot synthesis of thiol-functionalized mesoporous silica submicrospheres for Tl(I) adsorption: Isotherm, kinetic and thermodynamic studies. J. Hazard. Mater. 371, 146–155. https://doi.org/10.1016/j.jhazmat.2019.02.076.

Li, R., Hu, Z., Shao, X., Cheng, P., Li, S., Yu, W., Lin, W., Yuan, D., 2016. Large scale synthesis of NiCo layered double hydroxides for superior asymmetric electrochemical capacitor. Sci. Rep. 6, 1–9. https://doi.org/10.1038/srep18737.

Decoste, J.B., Peterson, G.W., Jasuja, H., Glover, T.G., Huang, Y.G., Walton, K.S., 2013. Stability and degradation mechanisms of metal-organic frameworks containing the $Zr_6O_4(OH)_4$ secondary building unit. J. Mater. Chem. A 1, 5642–5650. https://doi.org/10.1039/c3ta10662d.

Cavka, J.H., Jakobsen, S., Olsbye, U., Guillou, N., Lamberti, C., Bordiga, S., Lillerud, K.P., 2008. A new zirconium inorganic building brick forming metal organic frameworks with exceptional stability. J. Am. Chem. Soc. 130, 13850–13851. https://doi.org/10.1021/ja8057953.

Glocheux, Y., Albadarin, A.B., Galán, J., Oyedoh, E., Mangwandi, C., Gérente, C., Allen, S.J., Walker, G.M., 2014. Adsorption study using optimised 3D organised mesoporous silica coated with Fe and Al oxides for specific As(III) and As(V) removal from contaminated synthetic groundwater. Microporous Mesoporous Mater. 198, 101–114. https://doi.org/10.1016/j.micromeso.2014.07.020.

Soltani, R., Marjani, A., Shirazian, S., 2019. Shell-in-shell monodispersed triamine-functionalized SiO_2 hollow microspheres with micro-mesostructured shells for highly efficient removal of heavy metals from aqueous solutions. J. Environ. Chem. Eng. 7. https://doi.org/10.1016/j.jece.2018.102832. 102832.

Redlich, O., Peterson, D.L., 1959. A useful adsorption isotherm 1024 1024 J. Phys. Chem. 63. https://doi.org/10.1021/j150576a611.

Hall, K.R., Eagleton, L.C., Acrivos, A., Vermeulen, T., 1966. Pore- and solid-diffusion kinetics in fixed-bed adsorption under constant-pattern conditions. Ind. Eng. Chem. Fundam. 5, 212–223. https://doi.org/10.1021/i160018a011.

Zhang, G., Fan, F., Li, X., Qi, J., Chen, Y., 2018. Superior adsorption of thallium(I) on titanium peroxide: Performance and mechanism. Chem. Eng. J. 331, 471–479. https://doi.org/10.1016/j.cej.2017.08.053.

Li, H., Li, X., Xiao, T., Chen, Y., Long, J., Zhang, G., Zhang, P., Li, C., Zhuang, L., Li, K., 2018. Efficient removal of thallium(I) from wastewater using flower-like manganese dioxide coated magnetic pyrite cinder. Chem. Eng. J. 353, 867–877. https://doi.org/10.1016/j.cej.2018.07.169.

Li, H., Chen, Y., Long, J., Li, X., Jiang, D., Zhang, P., Qi, J., Huang, X., Liu, J., Xu, R., Gong, J., 2017. Removal of thallium from aqueous solutions using Fe-Mn binary oxides. J. Hazard. Mater. 338, 296–305. https://doi.org/10.1016/j.jhazmat.2017.05.033.

Zhang, L., Huang, T., Zhang, M., Guo, X., Yuan, Z., 2008. Studies on the capability and behavior of adsorption of thallium on nano-Al_2O_3. J. Hazard. Mater. 157, 352–357. https://doi.org/10.1016/j.jhazmat.2008.01.005.

Lima, E.C., Hosseini-Bandegharaei, A., Moreno-Piraján, J.C., Anastopoulos, I., 2019. A critical review of the estimation of the thermodynamic parameters on adsorption equilibria. Wrong use of equilibrium constant in the Van't Hoof equation for calculation of thermodynamic parameters of adsorption. J. Mol. Liq. 273, 425–434. https://doi.org/10.1016/j.molliq.2018.10.048.

Zhou, Y., Zhang, M., Wang, X., Huang, Q., Min, Y., Ma, T., Niu, J., 2014. Removal of crystal violet by a novel cellulose-based adsorbent: Comparison with native cellulose. Ind. Eng. Chem. Res. 53, 5498–5506. https://doi.org/10.1021/ie404135y.